

Coarse Grained Molecular Simulation of Exosome Squeezing for Drug Loading

Khayrul Islam ^a, Meghdad Razizadeh ^b and Yaling Liu ^{a, c}

^a Department of Mechanical Engineering and Mechanics, Lehigh University, Bethlehem, Pennsylvania 18015, USA.

^b Department of Developmental Neurobiology, St. Jude Children's Research Hospital, Memphis, TN 38105, USA.

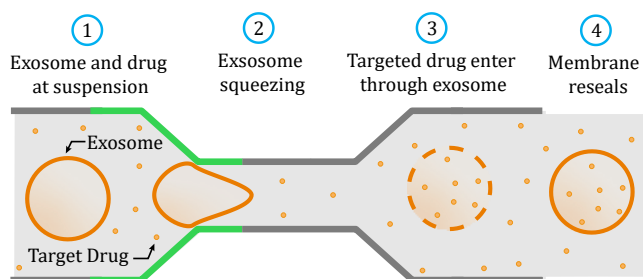
^c Department of Bioengineering, Lehigh University, Bethlehem, Pennsylvania 18015, USA.

KEYWORDS:

Exosome, Coarse-grain simulation, Nanochannel, Squeezing, Drug loading, Molecular dynamics

ABSTRACT

In recent years, extracellular vesicles such as exosomes have become promising carriers as the next-generation drug delivery platforms.



Effective loading of exogenous cargos without compromising the extracellular vesicle membrane is a major challenge. Rapid squeezing through nanofluidic channels is a widely used approach to load exogenous cargoes into the exosome through the nanopores generated temporarily on the membrane. However, the exact mechanism and dynamics of nanopores opening, as well as cargo loading through nanopores during the squeezing process remains unknown and is impossible to be visualized or quantified experimentally due to the small size of the exosome and the fast transient process. This paper developed a systemic algorithm to simulate nanopore formation and predict drug loading during exosome squeezing by leveraging the power of coarse-grain (CG) molecular dynamics simulations with fluid dynamics. The exosome CG beads are coupled with implicit Fluctuating Lattice Boltzmann solvent. Effects of exosome property and various squeezing test parameters, such as exosome size, flow velocity, channel width, and length, on pore formation and drug loading efficiency are analyzed. Based on the simulation results, a phase diagram is provided as a design guidance for nanochannel geometry and squeezing velocity to generate pores on membrane without damaging the exosome. This method can be utilized to perform a parametric study to optimize the nanofluidic device configuration and flow setup to obtain desired drug loading into exosomes.

* Address correspondence to

Yal310@lehigh.edu.

Biomembranes are among the most crucial parts of every living organism. The complex structure of biomembranes is composed of various fluid-like amphiphilic phospholipid molecules, transmembrane proteins, and carbohydrates. Exosomes, a subtype of extracellular vesicle that contains fluid-like closed structures of phospholipids suspended in solutions, have wide application in biophysics and nanomedicine due to their similarity with natural biomembranes. For instance, exosomes are widely used as drug delivery vehicles.^{1,2} Being naturally derived composition and function as intracellular communication tools, they are free from several disadvantages compared to liposomal drug delivery, *e.g.*, endosomal degradation, immune clearance, organ toxicity, and insertional mutagenesis.³⁻⁶ Commonly used drug loading methods for exosomes include passive incubation and electroporation. Passive incubation has the drawback of long incubation time and low loading efficiency⁷⁻⁹ where electroporation can cause significant damage to both exosome and their cargos.^{7,8,10,11} Alternatively, nanofluidic squeezing can easily manipulate flow and samples of interest, thus showing great potential for exosome drug loading.^{12,13} The process includes mixing exosome and drug suspension, injection through a microfluidic device, and squeezing exosomes through nanochannel to generate transient nanopores on the membrane, thus allowing targeted cargos to enter the exosome. Transporting cargo through the membrane is a diffusion process that continues until the pore heals if the saturation level is not reached.

Various experimental methods have been developed to study the diffusion of lipid bilayers¹⁴, deformations of vesicles^{15,16}, and membrane fusion.¹⁷ For instance, super-resolution imaging techniques have progressed significantly to investigate the dynamics of biological membranes.^{18,19} However, the pore formation and rupture of exosomes under large deformations are hard to be studied with experimental approaches due to their small scale and transient short time scales. The current experimental setup and testing conditions are still based on trial and error and are far from achieving the best loading performance. Various numerical

approaches have been developed during the last three decades to complement experimental understandings of biomembranes. While All Atomic (AA) modeling techniques are still progressing in terms of developing more efficient computational algorithms, more accurate force fields and advanced sampling techniques ^{20,21}, many biological phenomena are still not in the accessible range of AA approaches. Coarse-graining AA systems can significantly reduce degrees of freedom and accelerate system dynamics to model higher lengths and longer time scales. Chemical specificity preservative CG models such as MARTINI have been extensively employed to study the diffusion of lipid molecules ²², vesicle fusion, lipid rafting, ^{23,24} transmembrane protein aggregation, ^{25,26} and pore formation. ²⁷ To further push the accessible length and time scale, various supra coarse-grained models of lipid molecules in which only a few beads represent the whole lipid molecule have been developed. ^{28–33} In explicit solvent approaches, the solvent particles are modeled explicitly and the dynamics of systems are usually modeled by molecular dynamics (MD) or dissipative particle dynamics (DPD). ³⁴

In the explicit solvent methods, majority of the simulation time is devoted to the calculation of interactions among solvent particles. Thus, the implicit solvent approaches are more efficient at the cost of a reduction in accuracy due to neglecting solvent degrees of freedom. The implicit solvent model of Cooke and Deserno ³⁰ has been widely used in the simulation of membrane bending rigidity ³⁵, protein aggregation ³⁶, pore formation, ^{35,37} and membrane fission ³⁸. The implicit solvent CG models of Cooke and Deserno ³⁰ can be coupled with fluid flow domains thermalized with stochastic fluctuations to consider the hydrodynamics effects without modeling all the solvent degrees of freedom explicitly. For instance, Atzberger *et al.* ³⁹ and Wang *et al.* ⁴⁰ developed an immersed boundary fluctuating hydrodynamics method that can be coupled with an implicit solvent CG model. Sterpone *et al.* ⁴¹ developed a multiscale model with a CG protein model that was coupled with a lattice-Boltzmann ^{42,43} flow solver. In a

similar approach, Brandner *et al.* ⁴⁴ and Yu and Dutt ⁴⁵ coupled the fluctuating lattice Boltzmann method ⁴³ with the implicit solvent Dry MARTINI ²³ approach to study the self-assembly and aggregation of lipid bilayers and deformations of lipid vesicles under high shear rate flow. In addition to particle-based approaches, continuum scale models such as boundary element methods have also been employed in modeling the deformation of lipid vesicles in fluid flow.^{46,47} Helfrich's free energy model ⁴⁸ is usually used to find the bilayer response to hydrodynamic perturbations. However, such continuum scale models lack enough details to model the formation of pores or rupture and typically are only accurate at low deformation regimes.

In this study, coupling between a minimal CG model of a lipid bilayer with the fluctuating lattice-Boltzmann method is presented. The head-tail, implicit solvent, CG model of Cooke and Deserno ³⁰ was used to represent the lipid molecules by only one head and two tail particles. The CG particles were coupled with a thermalized lattice-Boltzmann fluid flow solver. Moreover, hydrodynamics was modeled by a computationally efficient, grid-based, lattice-Boltzmann method with good parallelization and scalability. By employing such a CG model and fluid flow solver, we could model the squeezing process of exosomes with a diameter of tens of nanometers under realistic flow rates in a large computational box of a few hundreds of nanometers. The developed model was used to study the deformation of exosomes due to squeezing, pore formation, and drug loading through the transient pores. Unlike the stain-based pore formation model ⁴⁹, the pore formation process is simulated explicitly through coarse grained molecular dynamics coupled with a Lattice-Boltzmann flow solver, yet with large dimensional and time scales far beyond the reach of traditional molecular dynamics simulations. A novel approach for predicting pore formation and drug loading through the exosome is presented by studying the effects of various squeezing parameters. This parametric

study will provide guidance for the development of better exosome drug loading conditions and devices.

RESULTS AND DISCUSSION

Effect of flow velocity on exosome squeezing and drug loading. The effect of squeezing velocity on drug loading is analyzed first. The magnitude of force applied on the LB points is tuned to archive the desired maximum velocity in the center of the channel. Three cases with different flow velocities at the center of the channel are considered: a low velocity of $V_1 = 300 \text{ mm/sec}$, a medium of $V_2 = 500 \text{ mm/sec}$ and a high velocity of $V_3 = 700 \text{ mm/sec}$.

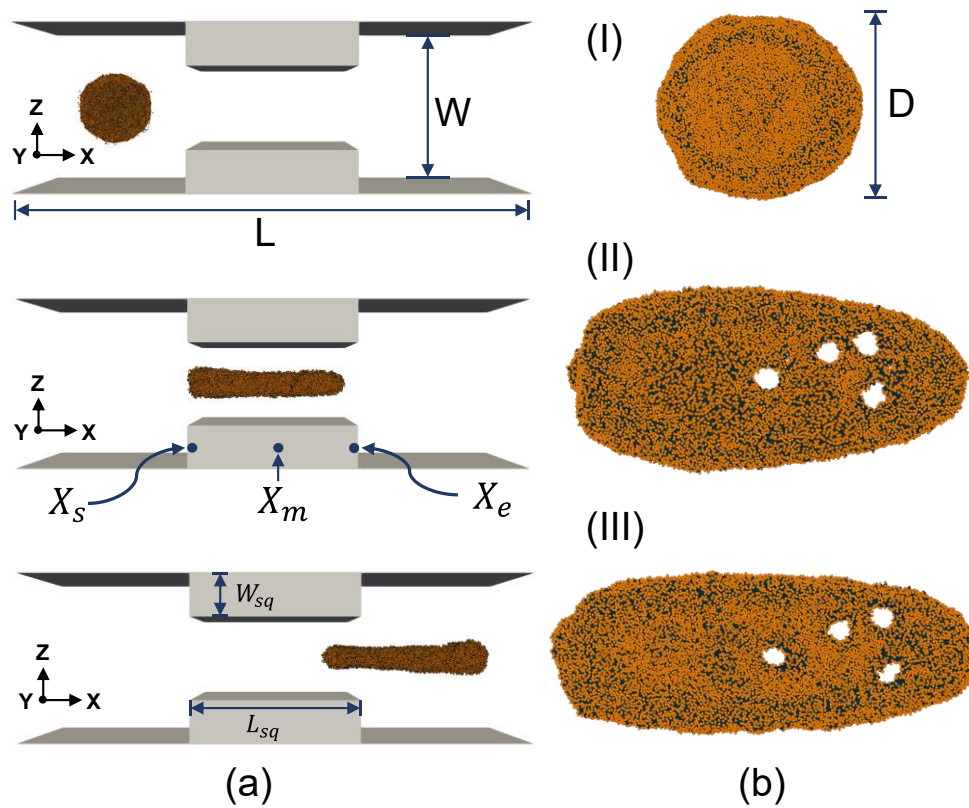


Figure 1: Exosome squeezing at a high flow velocity of 500 mm/sec. (a) Visualization of the simulation channel from XZ plane (b) molecular representation of exosome from XY plane. (I) Exosome at entrance location X_s , (II) Exosome at middle of squeezing channel X_m , (III) Exosome at exit location X_e .

The velocity range is physiologically meaningful and consistent with experimental results published by previous researchers^{50,51}. For all cases, other parameters are kept constant to compare the effect of the flow velocity on the exosome deformation. The channel length and width were fixed at $L=6D$ and $W=2D$ respectively, where D is the diameter of exosome. The constriction length L_{sq} and constriction width W_{sq} were $2D$ and $0.7D$ correspondingly.

Figure 1a shows the snapshot of exosome at different simulation points for V_2 case, namely before the exosome enter the squeezing channel (X_s), when the exosome was at the middle of the constriction channel (X_m) and at the exit of the constriction channel (X_e).

Figure 1b visualizes the molecular representation of the exosome for XY plane at the same time points indicated in

Figure 1a.

Figure 1b(II) and (III) visualize the pore opening due to the squeezing of the nanochannel.

Figure 2 visualizes the molecular representation of the pore opening for all the cases from the XY plane. It is visible from Figure 2 that with increasing velocity, the number of pores increases but the average pore radius decreases. Evans *et al.*⁵² suggested that an increased loading rate between 1-10 mN/m for lipid vesicles results in higher critical rupture tension. Membrane rupture is prone to occur when the membrane tension increases above the critical. Higher flow velocity through the nanochannel results in a higher loading rate for the membrane, and the critical tension for pore opening increases. This phenomenon increases the internal energy of the membrane, and when internal energy crosses the critical limit, it generates an unstable pore in the membrane. With increasing critical internal energy value, energy stored before pore opening increases. This high internal energy reduces the area per pore but increases the number of pores generated. A similar trend is observed in our previous work [85], where increased strain rate significantly increases total pore area but reduces average pore size. Under high strain rates, the membrane surface energy is released faster by generation of lots of small

pores rather than expanding existing pores. The complicated structure of the exosome tail can be related to the difference in velocity between the exosome tail center (located in the high-speed centerline area) and the tail edge (located near the wall). An increase in fluid velocity results in a more complicated tail structure as it increases the velocity difference between the center and edge of the tail. As squeezing velocity increases, deformed exosome vertical and horizontal diameter change increases accordingly due to the positive relationship between the cell deformability and the fluid driving force. Pore recovery is not modeled here due to the larger timescale of the pore recovery process compared to the simulation time scale.

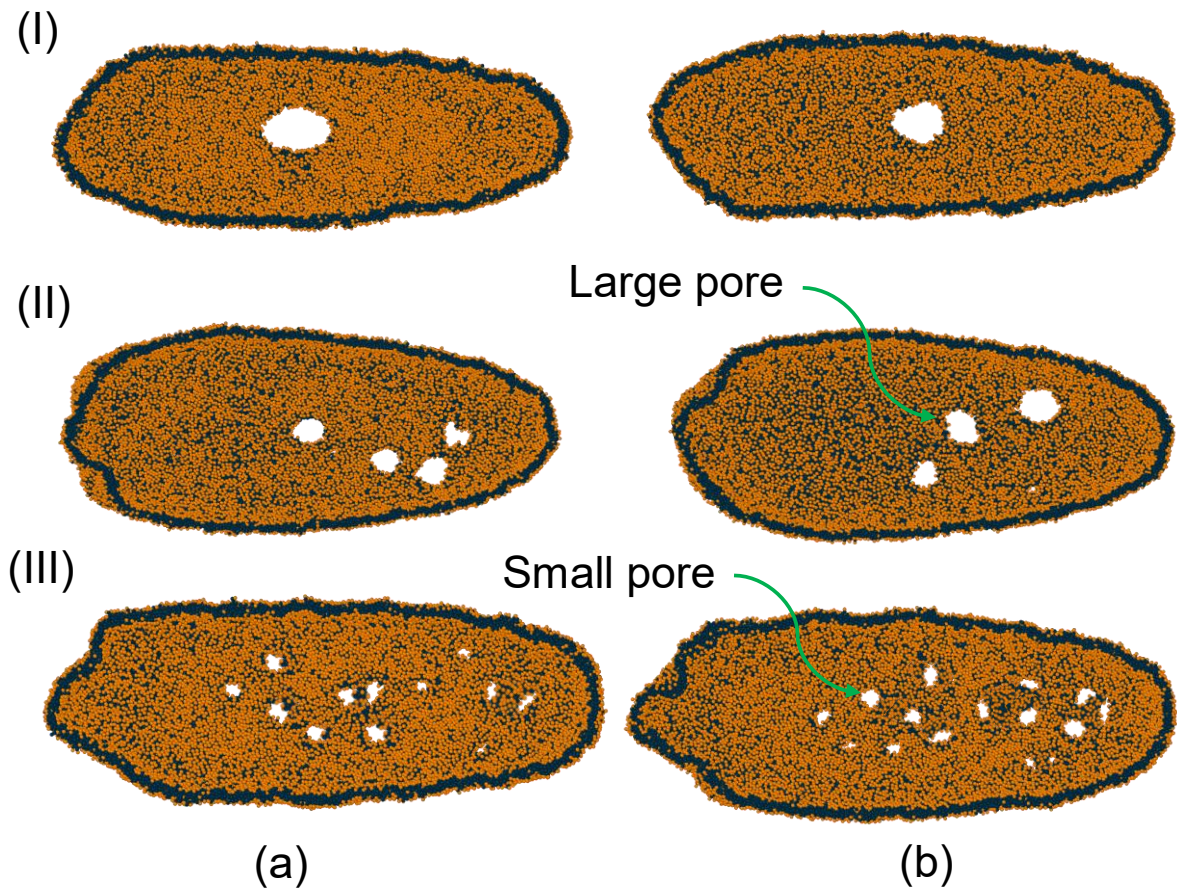


Figure 2: Squeezing of exosomes under various flow velocities. (a) XY plane top view (b) XY plane bottom view; (I) $V_1 = 300$ mm/sec , (II) $V_2 = 500$ mm/sec and (III) $V_3 = 700$ mm/sec.

The instantaneous cell diameter along the vertical and horizontal direction is plotted in Figure 3(a) and Figure 3 (b) respectively. The constriction region for the nanochannel is shown as the shaded region in all the graphs. The initial position for all simulations is fixed at $X_s = 80\sigma$. The change in exosome diameter is measured at the three zones described above. For all the cases, the horizontal diameter increases with the progression through the nanochannel.

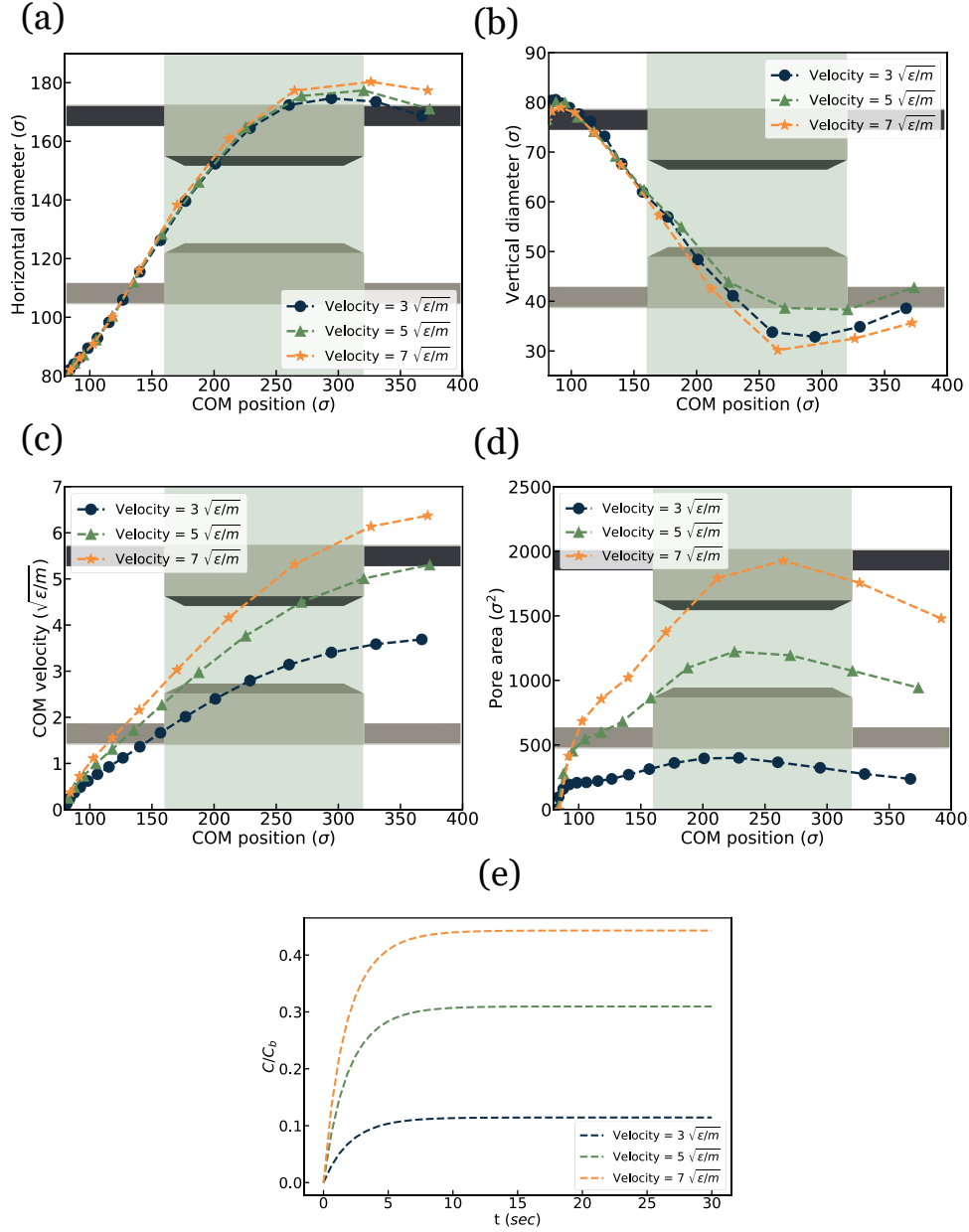


Figure 3: Simulation result under various flow velocities. (a) vertical diameter, (b) horizontal diameter, (c) Center of Mass (COM) velocity, and (d) Pore area vs. channel location (e) Drug loading over time.

In the beginning, the diameter changes at a lower rate, increasing up to the middle of the constriction. Then the exosome diameter change becomes stable during squeezing. For the rest of the channel, diameter decreases again as part of the exosome already passed the narrow

constriction. Vertical diameter shows an inverse trend in comparison to horizontal diameter. It starts with a slight decrease with a higher decrease in diameter up to the middle of the constriction. Then it shows a stable diameter followed by an increase in diameter at the end of the channel. With increasing flow velocity, horizontal diameter increases to a greater extent and vertical diameter decreases at the same rate as the volume of the exosome need to be constant. Figure 3(c) visualizes the change of Center of Mass (COM) velocity at different channel locations.

We observed an increase in COM velocity with a maximum velocity at the center of the constriction for all cases. The exosome velocity increases as the flow velocity increase at the center of the channel due to the constriction. The velocity profile observed here is consistent with the experimental value observed in Sharei *et al.*^{50,51,53} Due to exosome deformation, transient pores appear on the exosome membrane. Figure 3(d) visualizes the exosome pore area at different channel locations. The porosity of the exosome membrane increases until it reaches X_m . Subsequently, the porosity starts to decrease due to the recovery contraction of the cell membrane. The generation of transient pores shows a positive relationship with the flow velocity. With the increase in flow velocity, the pore area increases significantly. At the beginning of the exosome constriction, the area increases slowly, reaching a maximum value at the center. Afterward, the area again starts to decrease due to exosome shrinkage. Figure 4(e) represents the variation of drug loading rate within 30 sec of pore lifetime. The drug loading rate increases significantly with the flow velocity due to higher pore area generation. It is also visible from the graph that with the increase in flow velocity, the time required to reach the steady state also increases. This phenomenon is in agreement with the previous experimental results.^{50,51} Increase in flow velocity from V_1 to V_2 bumped up drug loading by ~200%, while an increase in velocity from V_2 to V_3 enhanced the drug loading by ~40%.

Effect of channel width on exosome squeezing and drug loading. We squeezed exosomes at different constriction widths to study the effect of channel width on drug loading. We have considered three constriction widths, *i.e.*, $W_1 = 0.6D$, $W_2 = 0.7D$, $W_3 = 0.8D$, where D is the diameter of the exosome. For all the cases, exosome velocity and constriction length are kept constant at $V_2 \approx 500 \text{ mm/sec}$ and $L=6D$ respectively. Exosome shapes at different channel locations are visualized in Figure 4. Exosome protrusion deformation is more apparent in narrower channels compared to the others. As we kept exosome average velocity identical for all the cases, exosomes required a greater driving force to go through the narrower channels. This phenomenon results in higher membrane stretch for narrower channels. The exosome tail has a more complex tail shape for higher driving force through the narrower channels, which causes a higher cell elongation towards the flow direction. It is observed from Figure 4 that narrower constriction causes the generation of a larger number of pores as well as a larger pore area. Exosome cells expand along the flow direction until they cross the narrow constriction. Afterward, it starts to shrink and transient pores healing takes place. It is observed from Figure 4 (c) that although a narrower constriction creates more pores in the exosome, having an extremely narrower constriction can potentially damage the exosome permanently and stop the exosome from recovering to its original shape (See supplementary material for exosome damage criteria). Thus, designing constriction width for squeezing exosomes needs proper attention and the value needs to be optimal, facilitating desired drug loading while keeping the exosome recoverable.

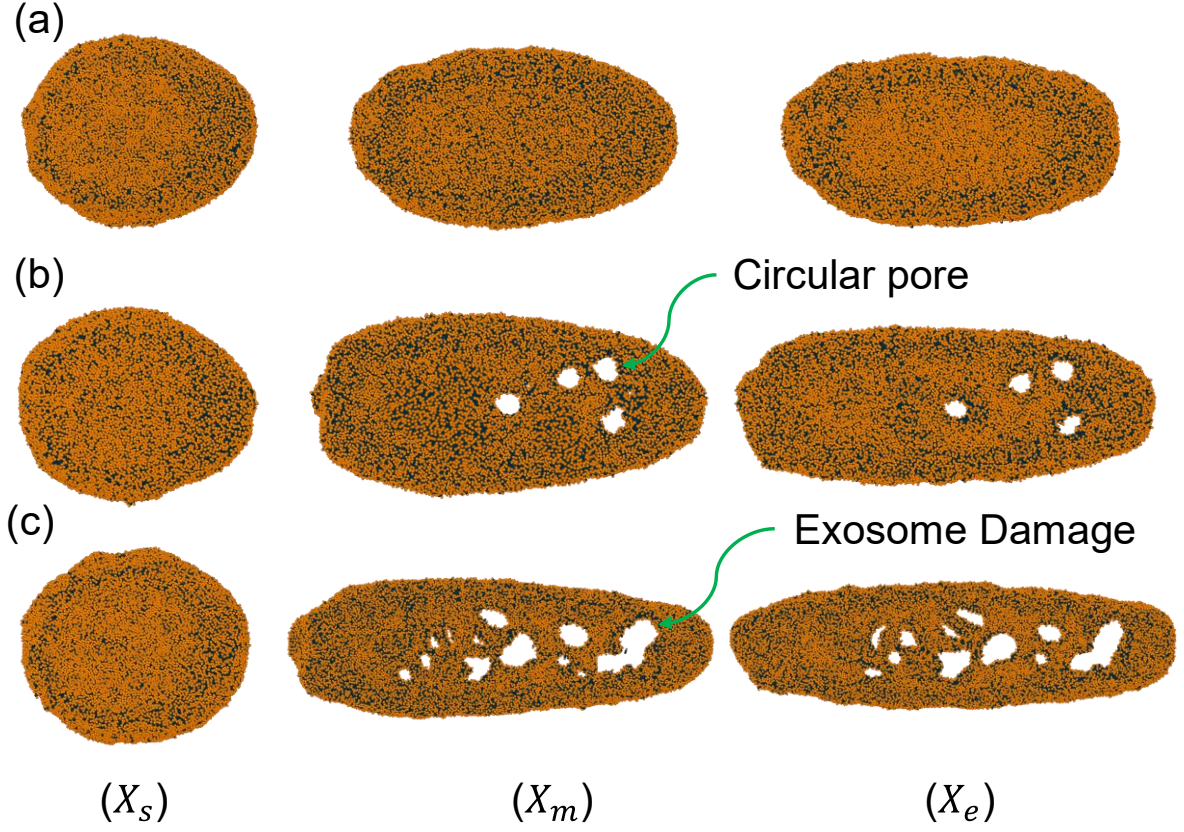


Figure 4: Exosome shape during squeezing at $V_2 \approx 500$ mm/sec and $L=6D$. (a) No pore under constriction width $W_{sq} = .8D \sigma$; (b) circular pore for constriction width $W_{sq} = .7D \sigma$; (c) Exosome damage for constriction width $W_{sq} = .6D \sigma$.

Figure 5(a) represents the change in horizontal diameter as a function of COM location along the channel. In all graphs, the constriction regions are shaded zone. All the graphs indicate a similar trend, as discussed in section 3(a). It shows a similar trend of increase in horizontal diameter as it propagates through the constriction, which is consistent with Figure 4. With the increase in channel constriction, a decrease in the exosome diameter becomes more prominent as it faces more driving force to go through the constriction. Figure 5(b) shows that as the horizontal diameter increases, the vertical diameter decreases as exosomes move along the channel due to the conservation of volume. Exosome velocity as a function of COM location for different constriction widths is illustrated in Figure 5(c).

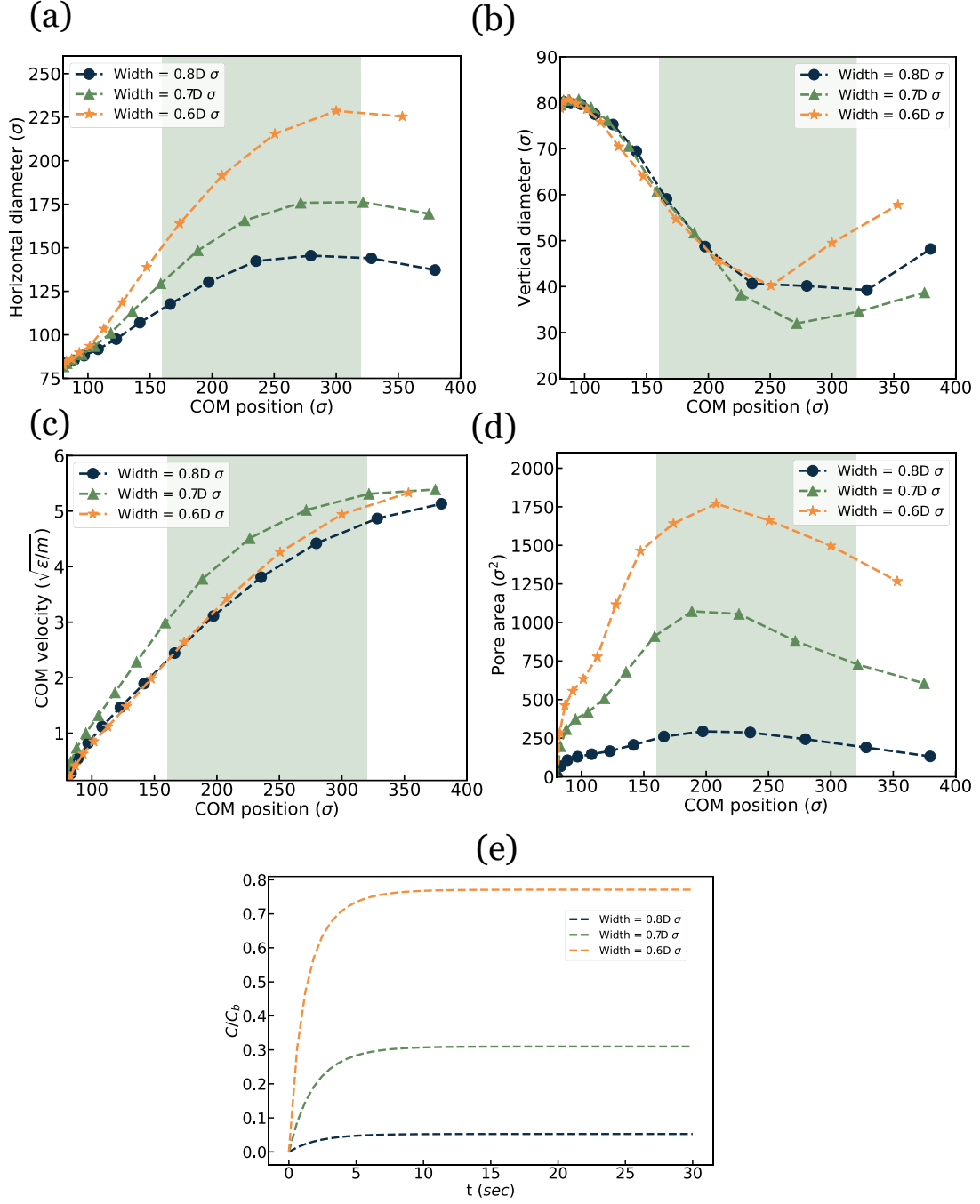


Figure 5: Exosome squeezing simulation result under various channel widths. (a) vertical diameter, (b) horizontal diameter, (c) Center of Mass (COM) velocity, (d) Pore area vs. channel location, (e) Drug loading over time.

Exosome drug loading increases at a higher rate for reduced constriction than in the other cases due to higher flow velocity. However, the difference in COM velocity for various

constrictions is minimal as the fluid inlet velocity for the channel was kept constant for all cases. Figure 5(c) represents the change in pore area for different cases of channel constriction. As observed in Figure 4, the number of pores generated in narrower constriction is higher than in others. This occurrence results in a larger pore area for narrower constriction, as shown in Figure 5(d). The normalized drug concentration inside the exosome cell is visualized in Figure 5(e). Drug concentration has a positive relationship with porosity and an increase in porosity results in higher drug concentration inside the exosome. This trend is consistent with previously published results from Sharei *et. al.*^{50,51} It should be mentioned that decreasing constriction from 0.7D to 0.6D results in more drug concentration in the exosome compared to the change from 0.8D to 0.7D. Reducing constriction from 0.8D to 0.7D results in a ~500% increase in drug concentration, whereas a change in constriction from 0.7D to 0.6D causes a ~166% increase.

Effect of exosome diameter on exosome squeezing and drug loading. This section analyzes the effect of exosome diameter on pore formation and drug loading. We have simulated three cases with different exosome diameter $D_1 = 60\sigma$, $D_2 = 70\sigma$ and $D_3 = 80\sigma$. All the channel length is kept constant at 6D to keep the exosome diameter to channel geometry ratio fixed. Here D is the diameter of the exosome. For each case, the exosome is positioned at $X = 1D$ location. The constriction length of 2D is considered in the middle of the channel. All the other parameters like flow velocity are kept constant at $V_2 \approx 500 \text{ mm/sec}$ and $L=6D$ respectively. Cell shapes at different channel locations are illustrated in Figure 6. As shown in the figure exosome with 60σ diameter does not have any visible pore whereas 70σ diameter exosome showed only 3 nanopores on the top view of the membrane. On the other hand, 80σ diameter exosome shows 4 nanopores, and pore areas are more prominent than in all other cases. The increase in exosome diameter shows a more complex tail geometry as it has a higher membrane area that deforms easily compared to the exosome with a lower membrane area.

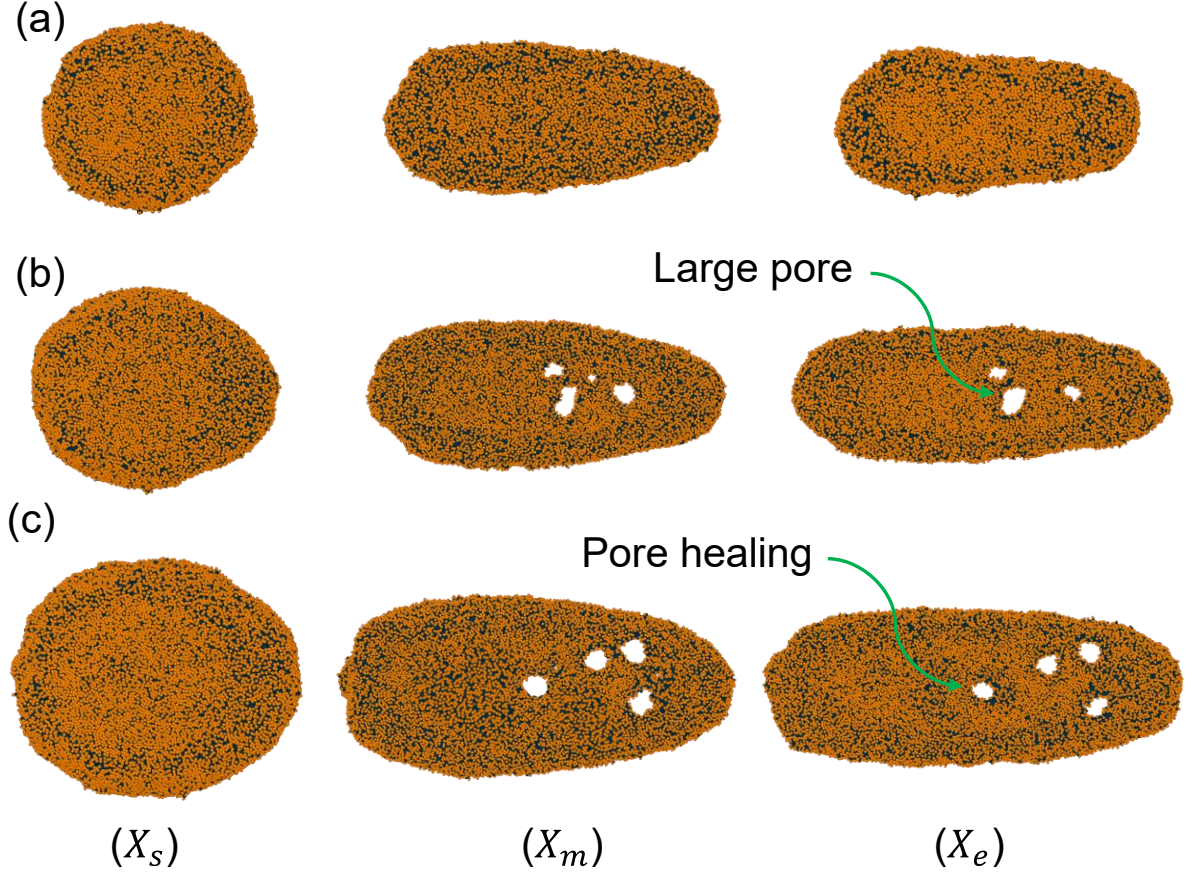


Figure 6: Exosome shape during squeezing at $V_2 \approx 500 \text{ mm/sec}$ and $L=6D$ for various exosome sizes. (a) exosome diameter $D = 60 \sigma$, (b) exosome diameter $D = 70 \sigma$, (c) exosome diameter $D = 80 \sigma$.

The horizontal diameter of exosome at different COM positions is visualized in Figure 7(a). Each graph starts from a different starting point as we positioned them at $X=1D$ to keep the diameter to channel length ratio constant. Each case has a constriction region of $2D$ shaded with different colors on all graphs. Exosome with a larger diameter has a larger expansion deformation than the other cases. Figure 7(b) illustrates the decrease in vertical diameter as a function of COM position. The exosome's vertical diameter development decreases as it passes through the narrow constriction due to the conservation of volume. Figure 7(c) visualizes the change in COM velocity for different exosome diameters.

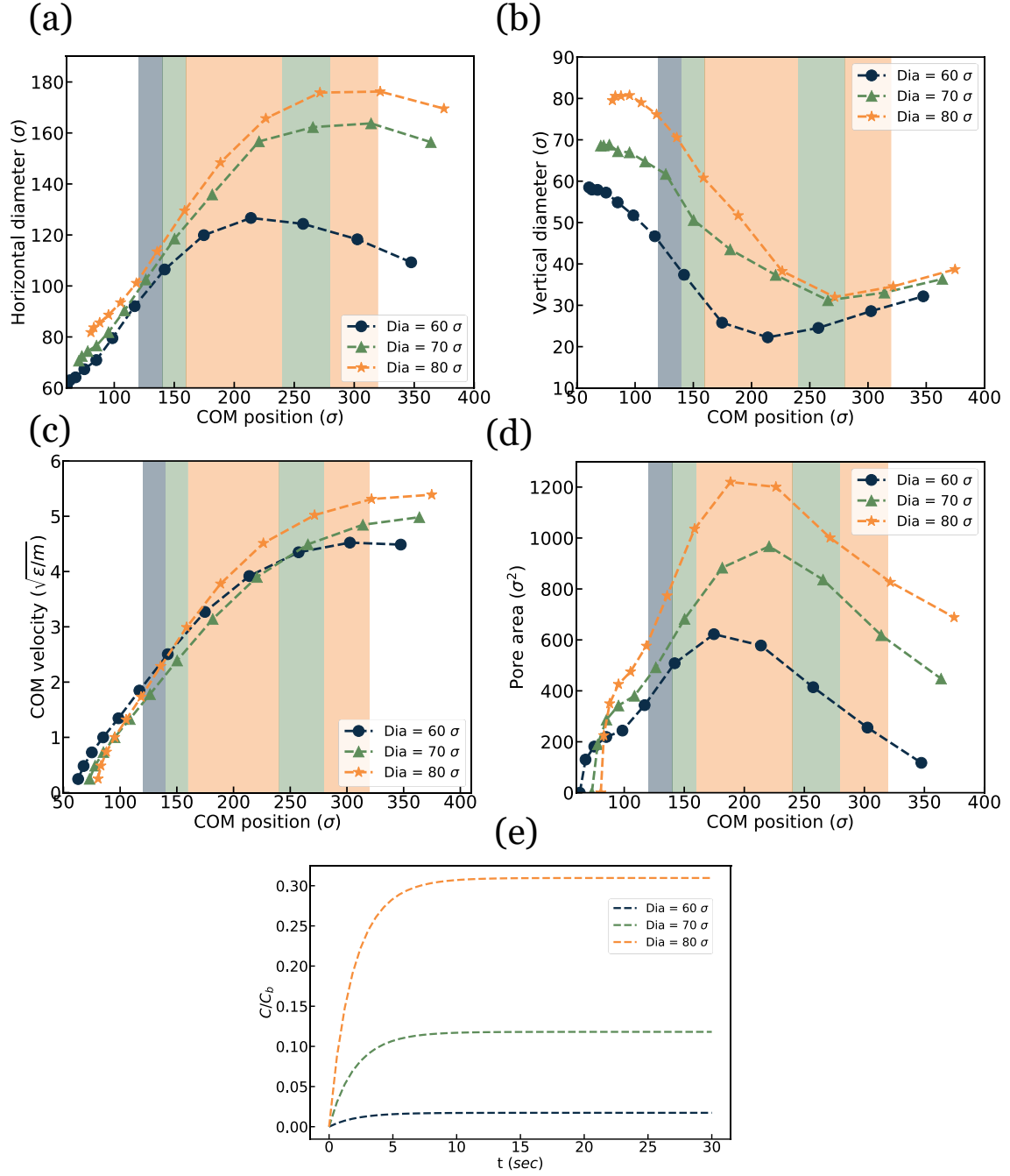


Figure 7: Exosome squeezing simulation result for exosome of various diameters. (a) vertical diameter, (b) horizontal diameter, (c) Center of Mass (COM) velocity, (d) Pore area vs. channel location, and (e) Drug loading over time.

The pore area for exosomes of different diameters is presented in Figure 7(d). It is observed that the exosome with a larger diameter has a larger pore area compared to the smaller diameter

counterparts. It should be mentioned that the exosome with $D_1 = 60\sigma$ in Figure 6 shows no pore in molecular representation. However, using the Delaunay tessellation method, surface representation showed some transient pore and the pore area for drug loading is calculated based on that post analysis. The normalized drug concentration inside the exosome cell is visualized in Figure 7(e). Drug concentration has a positive relation between porosity and an increase in porosity resulting in higher drug concentration inside the exosome.

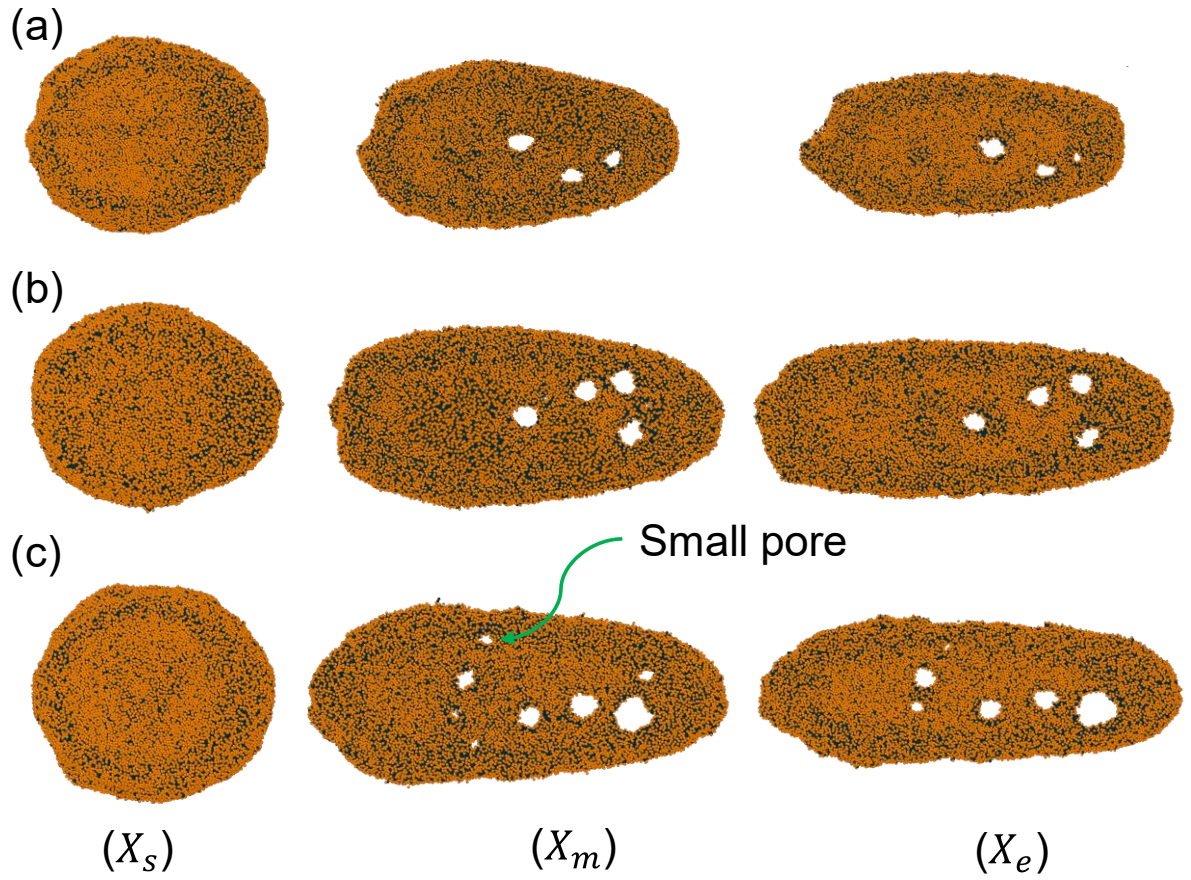


Figure 8: Exosome shape and pore formation during squeezing at : $V \approx 500 \text{ mm/sec}$ and $W=0.7D$ for various channel lengths (a) Very few pores for constriction length $L_{sq} = 1D$, (b) medium size pores for constriction length $L_{sq} = 2D$, (c) small and large pore for constriction length $L_{sq} = 3D$.

Effect of channel length on exosome squeezing and drug loading. Lastly, we checked the effect of squeezing length/duration on exosome drug loading by varying constriction length from $L_{sq_1} = 1D$, $L_{sq_2} = 2D$ and $L_{sq_3} = 3D$. The channel length is chosen as $L_1 = 5D$, $L_2 = 6D$ and $L_3 = 7D$ to keep the inlet and outlet distance constant for all cases. All the other parameters like flow velocity and channel width are kept constant at $V_2 \approx 500 \text{ mm/sec}$ and $W=2D$ respectively. Cell shapes at different channel locations are illustrated in Figure 8. The cell dynamics and deformation are pretty similar to that described in the previous sections. As shown in Figure 8, the exosome deformation is larger for greater constriction lengths.

Figure 9(a) shows the change in exosome diameter as a function of COM position. The exosome diameter changes with increased constriction length. In Figure 9(b), we observe an opposite relationship between the vertical diameter and constriction length consistent with the abovementioned results. Exosome COM velocity as a function of COM position is visualized in Figure 9(c) where the trend is almost the same for all cases.

As shown in Figure 9(d) pore area increases as the constriction length increases which is also observed in Figure 8 and is consistent with the result above. Finally, Figure 9(e) shows the normalized drug concentration inside the exosome with respect to loading time. It suggests that drug loading is a function of channel length; a longer channel leads to higher normalized drug loading. Therefore, the result is consistent with experimental findings^{50,51} suggesting that higher loaded drug concentration can be achieved by increased squeezing channel length.

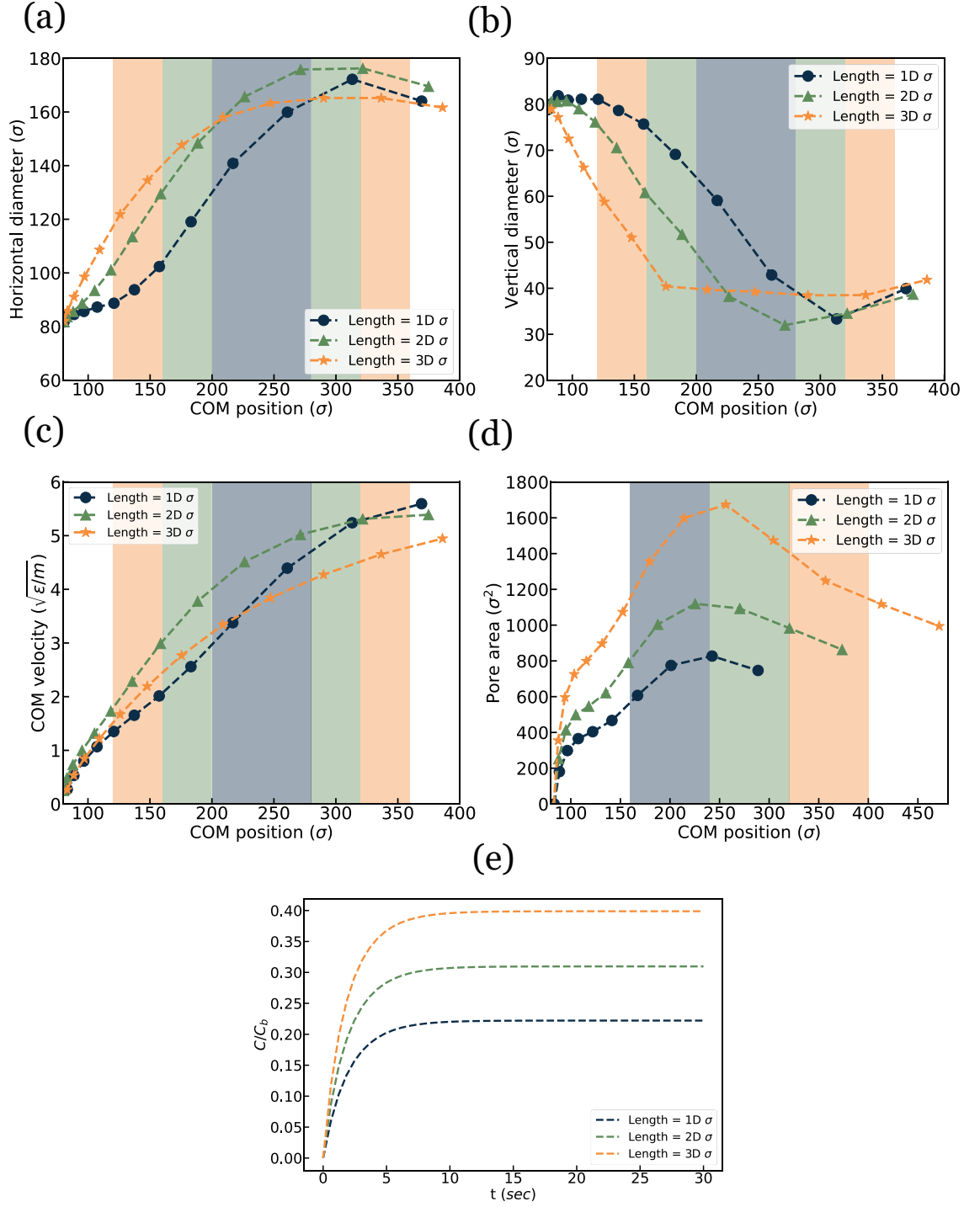


Figure 9: Exosome squeezing simulation results under various channel lengths. (a) vertical diameter, (b) horizontal diameter, (c) Center of Mass (COM) velocity, and (d) Pore area vs. channel location (e) Drug loading over time.

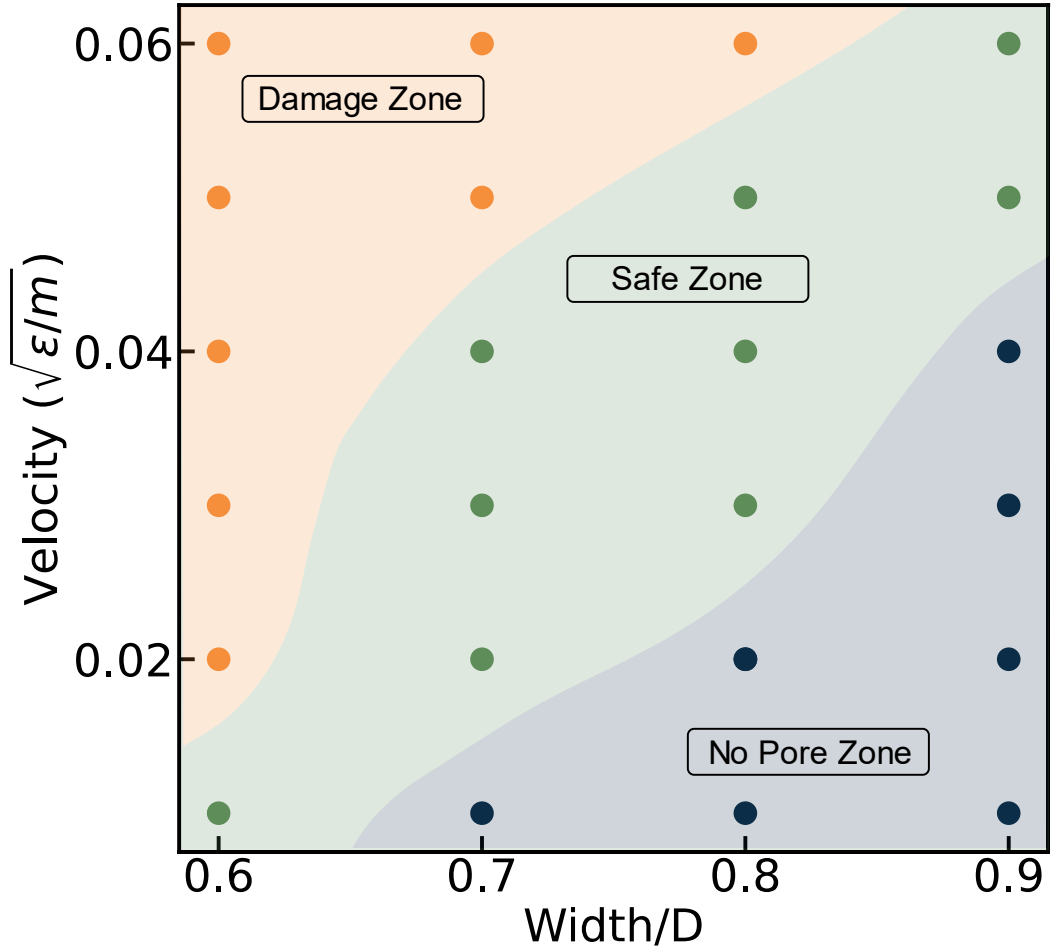


Figure 10: Phase diagram of pore formation status under different exosome velocities and constriction widths. Damage zone is where permanent damage or rupture happens on exosome. No pore zone is where there is no pore formation on exosome. Safe zone is the suggested status where transient pores are formed on exosome enabling drug loading.

To provide guidance on how to design proper channel geometry and exosome velocity for effective pore opening and drug loading, we performed simulations under a large range of exosome squeezing velocities and nanochannel widths. In Figure 10, a pore opening status phase diagram is generated as a function of exosome velocity and constriction width. We categorize exosome squeezing results into damage zone, safe zone, and no pore zone. Damage zone is where permanent damage or rupture happens on exosome. No pore zone is where there is no pore formation on exosome. Safe zone is the suggested status where transient pores are formed on exosome enabling drug loading. From the phase diagram, it is clear that lower

constriction width and higher exosome velocity can potentially damage the exosome, based on the criteria described in the supplementary material (Figure S1). On the other hand, squeezing the exosome with a higher width and lower exosome velocity results in no pore creation, thus no drug loading into the exosome. In between the above two zones is a safe zone that generate transient pores on exosome which is favorable for drug loading.

Figure 11 summarizes the maximum pore area for various cases presented above. The pore area under each parameter's lower, middle and higher value results were reported. The lower value for velocity is 300 mm/sec , with a median value of 500 mm/sec and a higher value of 700 mm/sec . Similarly, for the length case, the constriction length values are $1D$, $2D$ and $3D$ respectively. For the diameter case, the diameters are considered for 60σ , 70σ and 80σ respectively. Lastly, for the width case, the constriction widths of $0.6D$, $0.7D$ and $0.8D$ are considered respectively. The lower constriction width case shows an abnormally high maximum pore area. The observation is consistent with Figure 4 and results from the highly narrow constriction that causes the exosome to be damaged. Thus, the exosome drug loading is very sensitive to channel width change, followed by a change in flow velocity.

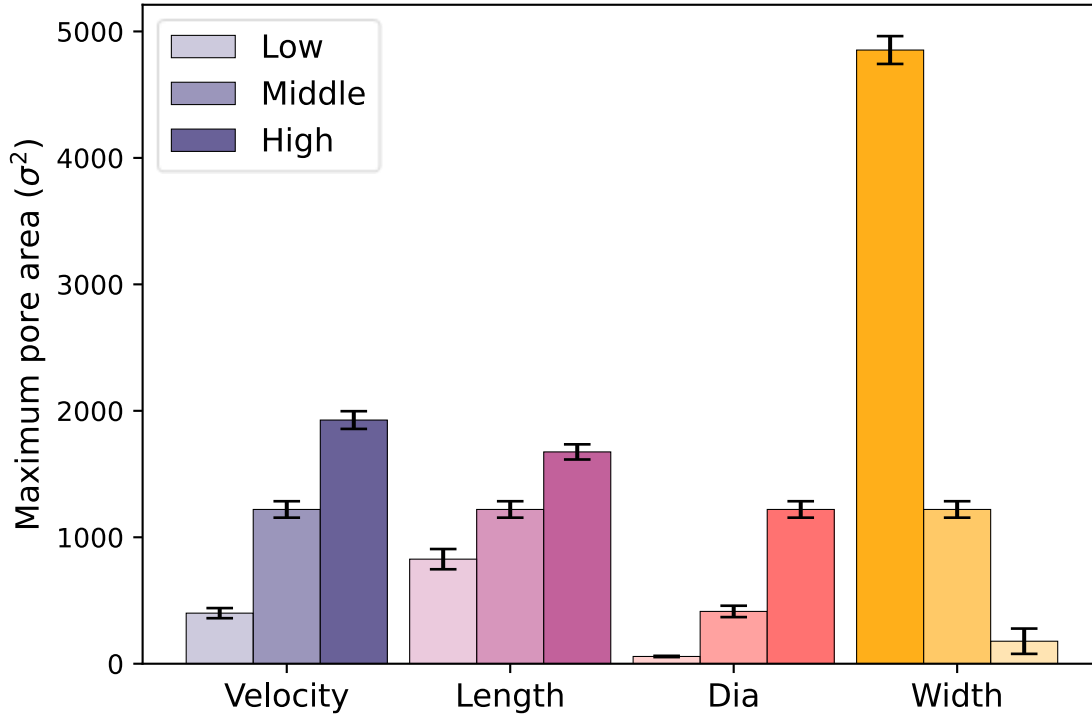


Figure 11: Summary of maximum pore area for exosome squeezing under various conditions.

CONCLUSION

We have coupled a computationally inexpensive supra CG model with fluctuating lattice-Boltzmann method, which enables us to simulate the entire exosome squeezing process with a reasonable computational cost. Each lipid molecule is represented by one head particle and two tail particles. In-house code is used to compute the pore formation and relate the pore area with drug loading through the diffusion process. The proposed method can predict the drug loading into the exosome and thus can help tune the squeezing parameters for desired drug loading. The method is free from any empirical parameter depending on operating conditions and channel geometry. Our results show that drug loading through the exosome increases with increasing flow velocity, increasing exosome diameter, decreasing constriction width, and increasing constriction length. An optimal value for channel width can be predicted to achieve maximum drug loading without damaging the exosome. Exosome squeezing through

nanochannel is a complicated phenomenon in biophysics; thus, the coarse-grained simulation presented in this work can provide insights into both the physics during the dynamic process and how various parameters influence drug loading. Exosome squeezing velocity, constriction width and length, properties of the exosome such as their sizes, shapes, and initial positions are parameters that can significantly change the loading results. In this model, we assume pores to be sealed after 30 s. However, pore closing time can differ depending on pore radius⁵⁴. We are working on developing a more efficient model that can simulate the pore closing with reasonable computational cost. The proposed model can be used to optimize squeezing parameters like flow velocity, channel geometry parameter and exosome diameter to obtain preferred drug loading through exosome.

METHODS

Simulation setup and parameters. In this study, we employed the implicit solvent CG model of Cooke and Deserno⁵⁵ to model the lipid vesicles where one hydrophilic head and two hydrophobic tail particles represent the lipid molecule (Figure 12 (c)). Weeks-Chandler-Anderson potential given by Eq. 1 governed all the interactions among particles.

$$v(r) = \begin{cases} 4\varepsilon \left[\left(\frac{\sigma}{r} \right)^{12} - \left(\frac{\sigma}{r} \right)^6 + 0.25 \right] & r \leq r_c \\ 0 & r \geq r_c \end{cases} \quad (1)$$

In which the ε and σ are the energy and length units of the system respectively. Here, r is the distance between two particles and r_c is the critical distance which is $r_c = 2^{1.2}\sigma$. We set $\sigma_{H-H} = \sigma_{H-T} = .95\sigma$ for the interactions of head particles and $\sigma_{H-H} = \sigma$ to ensure the cylindrical shape of lipid molecules. To represent the solvent effects, an attractive potential with the form of Eq. 2 with the range of w_c is added only to the tail particles.

$$v_{att}(r) = \begin{cases} -\varepsilon & r < r_c \\ -\varepsilon \cos^2\left(\frac{\pi(r - r_c)}{2w_c}\right) & r_c \leq r \leq r_c + w_c \\ 0 & r > r_c + w_c \end{cases} \quad (2)$$

The range of attractive interactions is tuned by the w_c parameter. This tunable parameter can affect the self-assembly and phase behavior of the lipid membrane and is set to $w_c = 1.6 \sigma$ in the rest of this study^{55–57}. Head and tail CG beads are bonded to each other with the finite extensible non-linear elastic (FENE) bond with the form of Eq. 3:

$$v_{bond}(r) = -\frac{1}{2}k_b r_0^2 \ln\left(1 - \left(\frac{r}{r_0}\right)^2\right) \quad (3)$$

In which the bond constant is $k_b = 30 \text{ } \epsilon/\sigma^2$ and the maximum bond length $r_0 = 1.5\sigma$. The lipid molecule is straightened by a harmonic angular potential of the form Eq. 4.

$$v_{bend}(\theta) = \frac{1}{2}k_a(\theta - \pi)^2 \quad (4)$$

In which the angle constant is $k_a = 10 \text{ } \epsilon/\text{rad}^2$ and θ is the angle made by the three CG beads of each lipid molecule. The hydrodynamic is solved by the lattice-Boltzmann equations^{58,59}.

A stochastic fluctuation term that conserves the local mass and momentum is added to the stress tensor to address critical thermal fluctuations at the nanoscale. Details of the stochastic term implementation can be found in the works of Ladd⁶⁰ and Dunweg and Ladd.⁶¹ We used the same grid size as the length unit of the CG model. Moreover, the time step is very similar to lattice-Boltzmann and MD simulations. The fluid domain is then coupled with the CG beads by a friction-based approach based on the implementation of Alrichs and Dunweg⁴³ in which

the velocities of the fluid domain are interpolated for each CG bead and the thermalized coupling force can be written as Eq. 5.

$$\vec{F} = -\gamma(\vec{u} - \vec{v}) + \vec{\chi} \quad (5)$$

The coupling is tuned by the friction parameter ζ . Here, \vec{u} and \vec{v} are the fluid and particle velocities respectively. $\vec{\chi}$ is a zero-mean stochastic force that satisfies Eq. 6:

$$\langle \chi_i(t) \chi_j(t') \rangle = 2\zeta k_B T \delta_{ij} \delta(t - t') \quad (6)$$

In which the k_B is the Boltzmann constant, T is the system temperature and δ is the Kronecker delta.

Each particle is assumed to have the same mass that makes the unit of time $\tau = \sqrt{\frac{m\sigma^2}{\epsilon}}$ reasonable. We aim to develop a standard algorithm to model exosome drug loading for different lipid conformations. Thus, the particles in our system do not correspond to any specific molecules, making the conversion to SI unit requires some interpretation. Each lipid tail can be considered a crude approximation of two-tail lipids, where each tail bead represents strands of five CH₂ groups. This assumption makes the length scale of the model $\sigma = .6 \text{ nm}$ and the mass scale of $N_A m \approx 140 \text{ g/mol}$. The temperature of the system is the same as body temperature, $T = 310 \text{ K}$ causes the units of energy being $\epsilon = 4.27 \times 10^{-21} \text{ J}$.

The number of beads used for creating the exosome varies between 44k~90k with a change of diameter, $60\sigma \sim 80\sigma$. The area per lipid for outer and inner leaflet is measured by dividing the surface area of the leaflet by the lipid head number for each leaflet. The equilibrated exosome has area per lipid (APL) at outer leaflet a^+ and inner leaflet a^- $1.1\sigma^2$ and $1.3\sigma^2$ respectively, which is very similar to Cooke and Deserno⁵⁷. The equilibrium APL in the outer and inner leaflet is different and the average APL is calculated by averaging the values. The average APL for the exosome is measured to be $a_{\text{avg}} = 1.2\sigma$. Choice of potential width w_c and temperature $K_B T$ are critical for defining the fluidity of the membrane. We choose w_c and

$K_B T$ value to be 1.6 and 1 respectively that to be in the fluidic phase to ensure in plane fluidity of the membrane. With the estimates of $\sigma = 0.6 \text{ nm}$ the calculated bilayer thickness is $\sim 2.64 \text{ nm}$. The measured value is less than the typical bilayer thickness of $\sim 5 \text{ nm}$, but it is still in the lower but acceptable range of the reported range of bilayer thickness⁶².

The exosome is created using an in-house script, maintaining equal distance between head beads and aligning the tails with the head of the lipid as visualized in Figure 12(a) and 2(b). Then the structure is equilibrated to get a stable stress-free configuration using Langevin thermostat with the temperature of $K_B T = 1\epsilon$ and timestep of 0.01τ for 500τ . The stress-free structure is verified by observing minimal potential energy with a fluctuation of $< 1\%$. Then the exosome is exposed to the fluid flow created through an implicit representation of fluid via the Lattice-Boltzmann Method (LBM) of the ESPResSo package.⁶³ LBM is the first and most efficient lattice-based method that can be coupled with molecular dynamics, enabling the inclusion of hydrodynamic interactions into the simulation. In this method, Poiseuille flow is created by applying a homogeneous external body force density to the fluid in the MD unit. The simulation setup is visualized in Figure 12(d) and (e).

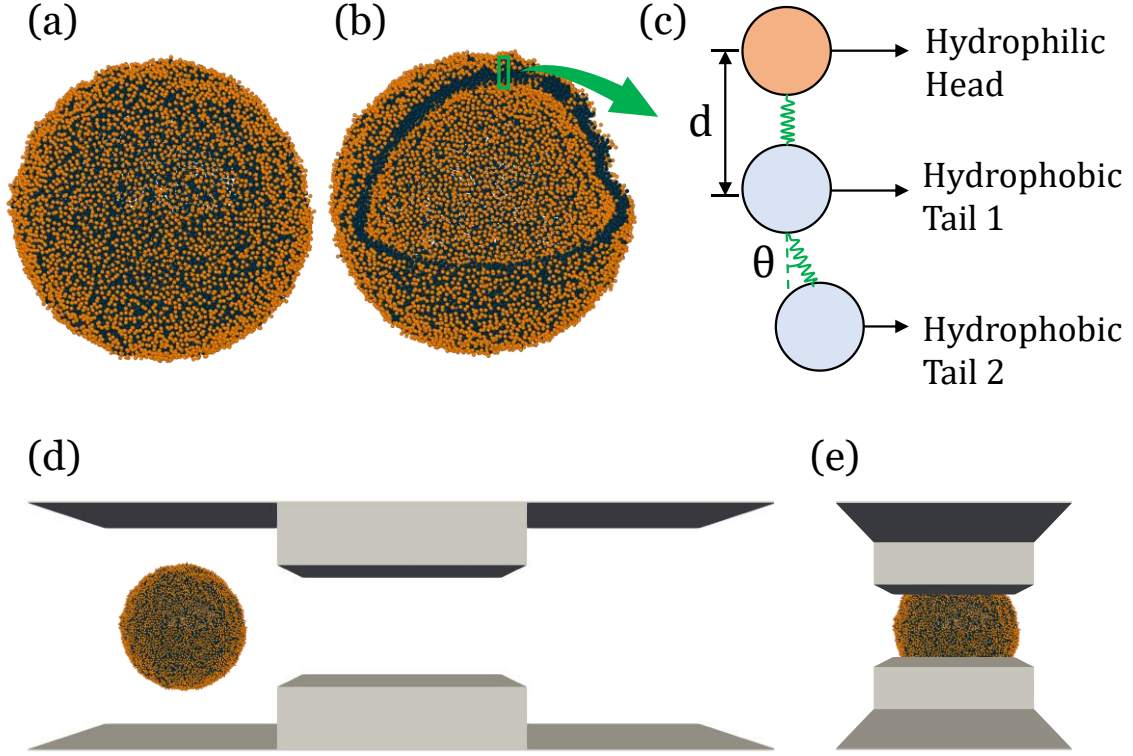


Figure 12: Simulation setup (a) XY view, (b) orthogonal view, (c) CG model of exosome, (d) and (e) simulation box with exosome

The flow in a nanochannel around the exosome is laminar. Reynolds number is maximum at the narrow channel where the fluid has maximum velocity. The Reynolds number (Re) is calculated as $Re = \frac{v\rho L}{\mu}$. Here L is the characteristic length of the channel, v is the velocity of the fluid, ρ the density of the fluid, and η the dynamic viscosity of the fluid. In our simulation, the characteristic or cord length of the largest rectangular channel is 160σ . Using the value of dynamic viscosity $\eta = 1.98 \pm 0.16\sigma^{-2}\sqrt{m\epsilon}$, $\rho = 0.8\sigma^3$ and highest velocity $v \approx 1.0\sqrt{\epsilon/m}$ maximum Reynolds number calculated as $Re = 564$.

Pore area and drug diffusion analysis. The drug loading largely depends on the formation of pores on the exosome surface, which needs to be accurately measured. However, it is difficult to calculate the size and area of the many pores formed on the exosome since these pores are voids enclosed by discrete CG beads. To quantitatively measure the area of many

pores formed on the exosome surface, we converted the bead representation of the exosome into a surface representation to analyze the pore formation. A triangulated surface mesh construction method developed by Stukowski ⁶⁴ is followed to convert the three-dimensional particle into a geometric surface. This method uses the Delaunay tessellation method to construct the surface based on particle coordinates. It tessellates the three-dimensional spaces into tetrahedral simplices, which are subsequently classified as either belonging to an empty or filled spatial region. Finally, it constructs the surface manifold that separates the empty and filled region of space. To assign each tetrahedral Delaunay element to either the filled or the empty region concept of a probe sphere with a suitable radius is implemented. The empty region is a collection of all spaces where the probe can fit without touching any particles. The remaining tetrahedral regions are considered filled regions. Thus, the value of this probe radius is critical to calculating the empty region, and the probe sphere radius selection needs some investigation. It depends on how much atomic detail we want to capture in the pore definition. A smaller probe radius enables the capture of more detailed features with the cost of computational power. In our system, we choose the probe radius to be 1 nm which is the same value as the first nearest neighbor found by calculating $g(r)$ value (see Figure S2 for surface representation of exosome using Delaunay tessellation method).

Sharei *et al.* ⁵¹ observed that the drug loading process happens within the first minute of the treatment process. This reported time scale for this process is independent of the empirical parameters and system design. Also, according to McNeil and Steinhardt ⁶⁵, it takes around 30 sec for the membrane to recover after transient pore opening. Previous work on pore dynamics suggested a longer pore opening time for largely deformed membranes under high-speed stretching. Therefore, assuming that the exosome reaches maximum porosity during squeezing is reasonable. Based on experimental observation, we believe all pores will be healed

after 30 sec following an exponential decay function regardless of their shape and size. The exponential decay function can be defined as:

$$A_{pore} = A_{max}^o \exp(-\gamma t) \quad (7)$$

Here A_{max}^o is maximum pore area calculated right after squeezing, γ is the decay constant and can be measured by considering $\frac{A_{pore}}{A_{max}^o} = 10^{-6}$ or a negligible value after 30 sec of squeezing. Drug loading inside the membrane is a diffusion process therefore, drug concentration inside the exosome can be governed as:

$$\frac{\delta C}{\delta t} = \nabla \cdot (D_{eff} \nabla C) \quad (8)$$

Where D_{eff} and C is the effective diffusion coefficient and drug concentration inside the exosome respectively. The effective diffusion coefficient is considered to be $3 \times 10^{-15} \text{ m/s}$ consistent with⁵¹. They obtained membrane diffusivity by simulating the diffusion of the delivery material into the cells suspended in a buffer of the delivery material. They also simulated the diffusion of material from the cell into a clean solution with no delivery material. The volume integral can be converted into a surface integral using the divergence theorem. A surface integral on the exosome surface can be approximated as:

$$\frac{\delta C}{\delta t} V_{exosome} = D_{eff} [(\nabla C)_{out} - (\nabla C)_{in}] A_{pore} \quad (9)$$

Here $(\nabla C)_{out}$ can be considered as zero as the concentration of the buffer can is higher than the concentration inside the exosome. Considering drug concentration C_b to be constant over time makes equation 9 further simplified.

$$-(\nabla C)_{in} = \frac{C_b - C}{L(\epsilon_A)} \quad (10)$$

Where L is the membrane thickness of exosomes determined as a function of areal strain. More details on the calculation of membrane thickness can be found in our previous article⁶⁶. By substituting equation 10 into equation 9 and solving the ordinary differential equation (ODE) with an initial condition $C=0$ at $t=0$ we get

$$\frac{c}{c_b} = 1 - \exp \left[\frac{D_{eff} A^0}{\gamma V_{exosome} L(\epsilon_A)} (\exp(-\gamma t) - 1) \right] \quad (11)$$

Conflict of Interest: The authors declare no competing financial interest

Supplementary Information available: See the supplementary material for the exosome damage criteria

Authors' Contributions: K.I. designed research, performed research, analyzed data, and wrote the paper. M.R. designed research and wrote the paper. Y.L. designed and directed research, performed research, analyzed data, and wrote the paper.

ACKNOWLEDGMENTS

This work was supported by National Institute of Health Grant R01HL131750, R21EB033102, National Science Foundation Grant CBET 2039310, EECS 2215789, Pennsylvania Department of Health Commonwealth Universal Research Enhancement Program (CURE), and Pennsylvania Infrastructure Technology Alliance (PITA).

REFERENCES AND NOTES

- (1) Stewart, M. P.; Sharei, A.; Ding, X.; Sahay, G.; Langer, R.; Jensen, K. F. In Vitro and Ex Vivo Strategies for Intracellular Delivery. *Nature* **2016**, *538* (7624), 183–192. <https://doi.org/10.1038/nature19764>.
- (2) Stewart, M. P.; Langer, R.; Jensen, K. F. Intracellular Delivery by Membrane Disruption: Mechanisms, Strategies, and Concepts. *Chem Rev* **2018**, *118* (16), 7409–7531. https://doi.org/10.1021/ACS.CHEMREV.7B00678/ASSET/IMAGES/MEDIUM/CR-2017-00678N_0045.GIF.
- (3) Jia, G.; Han, Y.; An, Y.; Ding, Y.; He, C.; Wang, X.; Tang, Q. NRP-1 Targeted and Cargo-Loaded Exosomes Facilitate Simultaneous Imaging and Therapy of Glioma in Vitro and in Vivo. *Biomaterials* **2018**, *178*, 302–316. <https://doi.org/10.1016/J.BIOMATERIALS.2018.06.029>.

- (4) He, G.; Feng, J.; Zhang, A.; Zhou, L.; Wen, R.; Wu, J.; Yang, C.; Yang, J.; Li, C.; Chen, D.; Wang, J.; Hu, N.; Xie, X. Multifunctional Branched Nanostraw-Electroporation Platform for Intracellular Regulation and Monitoring of Circulating Tumor Cells. *Nano Lett* **2019**, *19* (10), 7201–7209. <https://doi.org/10.1021/ACS.NANOLETT.9B02790>.
- (5) Kim, M. S.; Haney, M. J.; Zhao, Y.; Mahajan, V.; Deygen, I.; Klyachko, N. L.; Inskoe, E.; Piroyan, A.; Sokolsky, M.; Okolie, O.; Hingtgen, S. D.; Kabanov, A. v.; Batrakova, E. v. Development of Exosome-Encapsulated Paclitaxel to Overcome MDR in Cancer Cells. *Nanomedicine* **2016**, *12* (3), 655–664. <https://doi.org/10.1016/J.NANO.2015.10.012>.
- (6) Dixit, H. G.; Starr, R.; Dundon, M. L.; Pairs, P. I.; Yang, X.; Zhang, Y.; Nampe, D.; Ballas, C. B.; Tsutsui, H.; Forman, S. J.; Brown, C. E.; Rao, M. P. Massively-Parallelized, Deterministic Mechanoporation for Intracellular Delivery. *Nano Lett* **2020**, *20* (2), 860–867. https://doi.org/10.1021/ACS.NANOLETT.9B03175/SUPPL_FILE/NL9B03175_SI_001.PDF.
- (7) Rufino-Ramos, D.; Albuquerque, P. R.; Carmona, V.; Perfeito, R.; Nobre, R. J.; Pereira de Almeida, L. Extracellular Vesicles: Novel Promising Delivery Systems for Therapy of Brain Diseases. *J Control Release* **2017**, *262*, 247–258. <https://doi.org/10.1016/J.JCONREL.2017.07.001>.
- (8) Luan, X.; Sansanaphongpricha, K.; Myers, I.; Chen, H.; Yuan, H.; Sun, D. Engineering Exosomes as Refined Biological Nanoplatforams for Drug Delivery. *Acta Pharmacol Sin* **2017**, *38* (6), 754–763. <https://doi.org/10.1038/APS.2017.12>.
- (9) Sun, D.; Zhuang, X.; Xiang, X.; Liu, Y.; Zhang, S.; Liu, C.; Barnes, S.; Grizzle, W.; Miller, D.; Zhang, H. G. A Novel Nanoparticle Drug Delivery System: The Anti-Inflammatory Activity of Curcumin Is Enhanced When Encapsulated in Exosomes. *Mol Ther* **2010**, *18* (9), 1606–1614. <https://doi.org/10.1038/MT.2010.105>.
- (10) Nasiri Kenari, A.; Cheng, L.; Hill, A. F. Methods for Loading Therapeutics into Extracellular Vesicles and Generating Extracellular Vesicles Mimetic-Nanovesicles. *Methods* **2020**, *177*, 103–113. <https://doi.org/10.1016/J.YMETH.2020.01.001>.
- (11) Stewart, M. P.; Langer, R.; Jensen, K. F. Intracellular Delivery by Membrane Disruption: Mechanisms, Strategies, and Concepts. *Chem Rev* **2018**, *118* (16), 7409–7531. https://doi.org/10.1021/ACS.CHEMREV.7B00678/ASSET/IMAGES/MEDIUM/CR-2017-00678N_0045.GIF.
- (12) Xu, Y. Nanofluidics: A New Arena for Materials Science. *Advanced Materials* **2018**, *30* (3), 1702419. <https://doi.org/10.1002/ADMA.201702419>.
- (13) Rao, L.; Cai, B.; Bu, L. L.; Liao, Q. Q.; Guo, S. S.; Zhao, X. Z.; Dong, W. F.; Liu, W. Microfluidic Electroporation-Facilitated Synthesis of Erythrocyte Membrane-Coated Magnetic Nanoparticles for Enhanced Imaging-Guided Cancer Therapy. *ACS Nano* **2017**, *11* (4), 3496–3505. <https://doi.org/10.1021/ACSNANO.7B00133>.

- (14) Gaede, H. C.; Gawrisch, K. Lateral Diffusion Rates of Lipid, Water, and a Hydrophobic Drug in a Multilamellar Liposome. *Biophys J* **2003**, *85* (3), 1734–1740. [https://doi.org/10.1016/S0006-3495\(03\)74603-7](https://doi.org/10.1016/S0006-3495(03)74603-7).
- (15) Vitkova, V.; Mader, M.; Podgorski, T. Deformation of Vesicles Flowing through Capillaries. *Europhys Lett* **2004**, *68* (3), 398–404. <https://doi.org/10.1209/EPL/I2004-10211-9>.
- (16) Coupier, G.; Farutin, A.; Minetti, C.; Podgorski, T.; Misbah, C. Shape Diagram of Vesicles in Poiseuille Flow. *Phys Rev Lett* **2012**, *108* (17), 178106. <https://doi.org/10.1103/PHYSREVLETT.108.178106/FIGURES/6/MEDIUM>.
- (17) Shim, S. H.; Xia, C.; Zhong, G.; Babcock, H. P.; Vaughan, J. C.; Huang, B.; Wang, X.; Xu, C.; Bi, G. Q.; Zhuang, X. Super-Resolution Fluorescence Imaging of Organelles in Live Cells with Photoswitchable Membrane Probes. *Proc Natl Acad Sci U S A* **2012**, *109* (35), 13978–13983. https://doi.org/10.1073/PNAS.1201882109/-DCSUPPLEMENTAL/PNAS.1201882109_SI.PDF.
- (18) Zhanghao, K.; Liu, W.; Li, M.; Wu, Z.; Wang, X.; Chen, X.; Shan, C.; Wang, H.; Chen, X.; Dai, Q.; Xi, P.; Jin, D. High-Dimensional Super-Resolution Imaging Reveals Heterogeneity and Dynamics of Subcellular Lipid Membranes. *Nat Commun* **2020**, *11* (1). <https://doi.org/10.1038/S41467-020-19747-0>.
- (19) Sezgin, E. Super-Resolution Optical Microscopy for Studying Membrane Structure and Dynamics. *J Phys Condens Matter* **2017**, *29* (27). <https://doi.org/10.1088/1361-648X/AA7185>.
- (20) Neale, C.; Madill, C.; Rauscher, S.; Pomès, R. Accelerating Convergence in Molecular Dynamics Simulations of Solutes in Lipid Membranes by Conducting a Random Walk along the Bilayer Normal. *J Chem Theory Comput* **2013**, *9* (8), 3686–3703. https://doi.org/10.1021/CT301005B/SUPPL_FILE/CT301005B_SI_002.PDF.
- (21) Cherniavskiy, Y. K.; Fathizadeh, A.; Elber, R.; Tieleman, D. P. Computer Simulations of a Heterogeneous Membrane with Enhanced Sampling Techniques. *J Chem Phys* **2020**, *153* (14), 144110. <https://doi.org/10.1063/5.0014176>.
- (22) Vögele, M.; Köfinger, J.; Hummer, G. Hydrodynamics of Diffusion in Lipid Membrane Simulations. *Phys Rev Lett* **2018**, *120* (26), 268104. <https://doi.org/10.1103/PHYSREVLETT.120.268104/FIGURES/4/MEDIUM>.
- (23) Arnarez, C.; Uusitalo, J. J.; Masman, M. F.; Ingólfsson, H. I.; de Jong, D. H.; Melo, M. N.; Periole, X.; de Vries, A. H.; Marrink, S. J. Dry Martini, a Coarse-Grained Force Field for Lipid Membrane Simulations with Implicit Solvent. *J Chem Theory Comput* **2015**, *11* (1), 260–275. https://doi.org/10.1021/CT500477K/SUPPL_FILE/CT500477K_SI_002.PDF.
- (24) Barnoud, J.; Rossi, G.; Marrink, S. J.; Monticelli, L. Hydrophobic Compounds Reshape Membrane Domains. *PLoS Comput Biol* **2014**, *10* (10), e1003873. <https://doi.org/10.1371/JOURNAL.PCBI.1003873>.
- (25) Visscher, K. M.; Medeiros-Silva, J.; Mance, D.; Rodrigues, J. P. G. L. M.; Daniëls, M.; Bonvin, A. M. J. J.; Baldus, M.; Weingarth, M. Supramolecular Organization and

- Functional Implications of K⁺ Channel Clusters in Membranes. *Angew Chem Int Ed Engl* **2017**, 56 (43), 13222. <https://doi.org/10.1002/ANIE.201705723>.
- (26) Arnarez, C.; Marrink, S. J.; Periole, X. Molecular Mechanism of Cardiolipin-Mediated Assembly of Respiratory Chain Supercomplexes. *Chem Sci* **2016**, 7 (7), 4435–4443. <https://doi.org/10.1039/C5SC04664E>.
 - (27) Kirsch, S. A.; Böckmann, R. A. Membrane Pore Formation in Atomistic and Coarse-Grained Simulations. *Biochim Biophys Acta* **2016**, 1858 (10), 2266–2277. <https://doi.org/10.1016/J.BBAMEM.2015.12.031>.
 - (28) Goetz, R.; Gompper, G.; Lipowsky, R. Mobility and Elasticity of Self-Assembled Membranes. *Phys Rev Lett* **1999**, 82 (1), 221. <https://doi.org/10.1103/PhysRevLett.82.221>.
 - (29) Goetz, R.; Lipowsky, R. Computer Simulations of Bilayer Membranes: Self-Assembly and Interfacial Tension. *J Chem Phys* **1998**, 108 (17), 7397. <https://doi.org/10.1063/1.476160>.
 - (30) Cooke, I. R.; Kremer, K.; Deserno, M. Tunable Generic Model for Fluid Bilayer Membranes. *Phys Rev E Stat Nonlin Soft Matter Phys* **2005**, 72 (1), 011506. <https://doi.org/10.1103/PHYSREVE.72.011506/FIGURES/4/MEDIUM>.
 - (31) Drouffe, J. M.; Maggs, A. C.; Leibler, S. Computer Simulations of Self-Assembled Membranes. *Science* **1991**, 254 (5036), 1353–1356. <https://doi.org/10.1126/SCIENCE.1962193>.
 - (32) Ayton, G. S.; Voth, G. A. Hybrid Coarse-Graining Approach for Lipid Bilayers at Large Length and Time Scales. *Journal of Physical Chemistry B* **2009**, 113 (13), 4413–4424. <https://doi.org/10.1021/JP8087868>.
 - (33) Spangler, E. J.; Harvey, C. W.; Revalee, J. D.; Kumar, P. B. S.; Laradji, M. Computer Simulation of Cytoskeleton-Induced Blebbing in Lipid Membranes. *Phys Rev E Stat Nonlin Soft Matter Phys* **2011**, 84 (5), 051906. <https://doi.org/10.1103/PHYSREVE.84.051906/FIGURES/6/MEDIUM>.
 - (34) Ye, T.; Phan-Thien, N.; Lim, C. T. Particle-Based Simulations of Red Blood Cells-A Review. *J Biomech* **2016**, 49 (11), 2255–2266. <https://doi.org/10.1016/J.JBIOMECH.2015.11.050>.
 - (35) Deserno, M. Mesoscopic Membrane Physics: Concepts, Simulations, and Selected Applications. *Macromol Rapid Commun* **2009**, 30 (9–10), 752–771. <https://doi.org/10.1002/MARC.200900090>.
 - (36) Reynwar, B. J.; Illya, G.; Harmandaris, V. A.; Müller, M. M.; Kremer, K.; Deserno, M. Aggregation and Vesiculation of Membrane Proteins by Curvature-Mediated Interactions. *Nature* **2007**, 447 (7143), 461–464. <https://doi.org/10.1038/NATURE05840>.
 - (37) Illya, G.; Deserno, M. Coarse-Grained Simulation Studies of Peptide-Induced Pore Formation. *Biophys J* **2008**, 95 (9), 4163. <https://doi.org/10.1529/BIOPHYSJ.108.131300>.

- (38) Pannuzzo, M.; McDargh, Z. A.; Deserno, M. The Role of Scaffold Reshaping and Disassembly in Dynamin Driven Membrane Fission. *Elife* **2018**, *7*. <https://doi.org/10.7554/ELIFE.39441>.
- (39) Atzberger, P. J.; Kramer, P. R.; Peskin, C. S. A Stochastic Immersed Boundary Method for Fluid-Structure Dynamics at Microscopic Length Scales. *J Comput Phys* **2009**, *224* (2), 1255–1292. <https://doi.org/10.1016/j.jcp.2006.11.015>.
- (40) Wang, Y.; Sigurdsson, J. K.; Atzberger, P. J. Fluctuating Hydrodynamics Methods for Dynamic Coarse-Grained Implicit-Solvent Simulations in LAMMPS. <http://dx.doi.org/10.1137/15M1026390> **2016**, *38* (5), S62–S77. <https://doi.org/10.1137/15M1026390>.
- (41) Sterpone, F.; Derreumaux, P.; Melchionna, S. Protein Simulations in Fluids: Coupling the OPEP Coarse-Grained Force Field with Hydrodynamics. *J Chem Theory Comput* **2015**, *11* (4), 1843–1853. <https://doi.org/10.1021/CT501015H>.
- (42) Benzi, R.; Succi, S.; Vergassola, M. The Lattice Boltzmann Equation: Theory and Applications. *Phys Rep* **1992**, *222* (3), 145–197. [https://doi.org/10.1016/0370-1573\(92\)90090-M](https://doi.org/10.1016/0370-1573(92)90090-M).
- (43) Ahlrichs, P.; Dünweg, B. Simulation of a Single Polymer Chain in Solution by Combining Lattice Boltzmann and Molecular Dynamics. *J Chem Phys* **1999**, *111* (17), 8225. <https://doi.org/10.1063/1.480156>.
- (44) F. Brandner, A.; Timr, S.; Melchionna, S.; Derreumaux, P.; Baaden, M.; Sterpone, F. Modelling Lipid Systems in Fluid with Lattice Boltzmann Molecular Dynamics Simulations and Hydrodynamics. *Scientific Reports* **2019** *9:1* **2019**, *9* (1), 1–14. <https://doi.org/10.1038/s41598-019-52760-y>.
- (45) Yu, X.; Dutt, M. Implementation of Dynamic Coupling in Hybrid Molecular Dynamics–Lattice Boltzmann Approach: Modeling Aggregation of Amphiphiles. *Comput Phys Commun* **2020**, *257*. <https://doi.org/10.1016/J.CPC.2020.107287>.
- (46) Kaoui, B.; Tahiri, N.; Biben, T.; Ez-Zahraouy, H.; Benyoussef, A.; Biros, G.; Misbah, C. Complexity of Vesicle Microcirculation. *Phys Rev E Stat Nonlin Soft Matter Phys* **2011**, *84* (4), 041906. <https://doi.org/10.1103/PHYSREVE.84.041906>/FIGURES/6/MEDIUM.
- (47) Veerapaneni, S. K.; Rahimian, A.; Biros, G.; Zorin, D. A Fast Algorithm for Simulating Vesicle Flows in Three Dimensions. *J Comput Phys* **2011**, *230* (14), 5610–5634. <https://doi.org/10.1016/J.JCP.2011.03.045>.
- (48) Helfrich, W. Elastic Properties of Lipid Bilayers: Theory and Possible Experiments. *Z Naturforsch C* **1973**, *28* (11), 693–703. <https://doi.org/10.1515/ZNC-1973-11-1209>.
- (49) Nikfar, M.; Razizadeh, M.; Paul, R.; Zhou, Y.; Liu, Y. Numerical Simulation of Intracellular Drug Delivery via Rapid Squeezing. *Biomicrofluidics* **2021**, *15* (4), 044102. <https://doi.org/10.1063/5.0059165>.
- (50) Sharei, A.; Cho, N.; Mao, S.; Jackson, E.; Pocevičiute, R.; Adamo, A.; Zoldan, J.; Langer, R.; Jensen, K. F. Cell Squeezing as a Robust, Microfluidic Intracellular Delivery Platform. *J Vis Exp* **2013**, No. 81. <https://doi.org/10.3791/50980>.

- (51) Sharei, A.; Zoldan, J.; Adamo, A.; Sim, W. Y.; Cho, N.; Jackson, E.; Mao, S.; Schneider, S.; Han, M. J.; Lytton-Jean, A.; Basto, P. A.; Jhunjhunwala, S.; Lee, J.; Heller, D. A.; Kang, J. W.; Hartoularos, G. C.; Kim, K. S.; Anderson, D. G.; Langer, R.; Jensen, K. F. A Vector-Free Microfluidic Platform for Intracellular Delivery. *Proc Natl Acad Sci U S A* **2013**, *110* (6), 2082–2087. https://doi.org/10.1073/PNAS.1218705110/SUPPL_FILE/PNAS.201218705SI.PDF.
- (52) Evans, E.; Heinrich, V.; Ludwig, F.; Rawicz, W. Dynamic Tension Spectroscopy and Strength of Biomembranes. *Biophys J* **2003**, *85* (4), 2342–2350. [https://doi.org/10.1016/S0006-3495\(03\)74658-X](https://doi.org/10.1016/S0006-3495(03)74658-X).
- (53) Hao, R.; Yu, Z.; Du, J.; Hu, S.; Yuan, C.; Guo, H.; Zhang, Y.; Yang, H. A High-Throughput Nanofluidic Device for Exosome Nanoporation to Develop Cargo Delivery Vehicles. *Small* **2021**, *17* (35). <https://doi.org/10.1002/sml.202102150>.
- (54) Razizadeh, M.; Nikfar, M.; Paul, R.; Liu, Y. Coarse-Grained Modeling of Pore Dynamics on the Red Blood Cell Membrane under Large Deformations. *Biophys J* **2020**, *119* (3), 471–482. <https://doi.org/10.1016/j.bpj.2020.06.016>.
- (55) Cooke, I. R.; Kremer, K.; Deserno, M. Tunable Generic Model for Fluid Bilayer Membranes. *Phys Rev E Stat Nonlin Soft Matter Phys* **2005**, *72* (1). <https://doi.org/10.1103/PhysRevE.72.011506>.
- (56) Deserno, M. Mesoscopic Membrane Physics: Concepts, Simulations, and Selected Applications. *Macromol Rapid Commun* **2009**, *30* (9–10), 752–771. <https://doi.org/10.1002/marc.200900090>.
- (57) Cooke, I. R.; Deserno, M. Solvent-Free Model for Self-Assembling Fluid Bilayer Membranes: Stabilization of the Fluid Phase Based on Broad Attractive Tail Potentials. *Journal of Chemical Physics* **2005**, *123* (22). <https://doi.org/10.1063/1.2135785>.
- (58) Benzia, R.; Succib, S.; Vergassolac, M.; Succi, S. *THE LATTICE BOLTZMANN EQUATION: THEORY AND APPLICATIONS* The Lattke Boltzmann .Equation: Theory and Applications; 1992; Vol. 222.
- (59) Kushchenko, Y. K.; Belyaev, A. v. Effects of Hydrophobicity, Tethering and Size on Flow-Induced Activation of von Willebrand Factor Multimers. *J Theor Biol* **2020**, *485*. <https://doi.org/10.1016/J.JTBI.2019.110050>.
- (60) Ladd, A. J. Numerical Simulations of Particulate Suspensions via a Discretized Boltzmann Equation. Part 1. Theoretical Foundation. *J Fluid Mech* **1994**, *271*, 285–309. <https://doi.org/10.1017/S0022112094001771>.
- (61) Dünweg, B.; Ladd, A. J. C. Lattice Boltzmann Simulations of Soft Matter Systems. *Advances in Polymer Science* **2009**, *221* (1), 89–166. https://doi.org/10.1007/978-3-540-87706-6_2.
- (62) Harman, A.; Bertrand, M.; Joós, B. Deformation and Rupture of Vesicles Confined in Narrow Channels. *Can J Phys* **2017**, *95* (10), 916–922. <https://doi.org/10.1139/cjp-2016-0796>.
- (63) Weik, F.; Weeber, R.; Szuttor, K.; Breitsprecher, K.; de Graaf, J.; Kuron, M.; Landsgesell, J.; Menke, H.; Sean, D.; Holm, C. ESPResSo 4.0 – an Extensible Software

- Package for Simulating Soft Matter Systems. *European Physical Journal: Special Topics* **2019**, 227 (14), 1789–1816. <https://doi.org/10.1140/epjst/e2019-800186-9>.
- (64) Stukowski, A. Computational Analysis Methods in Atomistic Modeling of Crystals. *JOM* **2014**, 66 (3), 399–407. <https://doi.org/10.1007/s11837-013-0827-5>.
- (65) McNeil, P. L.; Steinhardt, R. A. Plasma Membrane Disruption: Repair, Prevention, Adaptation. <http://dx.doi.org/10.1146/annurev.cellbio.19.111301.140101> **2003**, 19, 697–731. <https://doi.org/10.1146/ANNUREV.CELLBIO.19.111301.140101>.
- (66) Sohrabi, S.; Liu, Y. A Cellular Model of Shear-Induced Hemolysis. *Artif Organs* **2017**, 41 (9), E80–E91. <https://doi.org/10.1111/AOR.12832>.